Hindawi
Advances in Materials Science and Engineering
Volume 2021, Article ID 5512782, 14 pages
https://doi.org/10.1155/2021/5512782

Research Article

Flexural Behavior of Innovative Posttensioned Composite Beams with Corrugated Steel Webs

Xiang Li,[1] **Tao Yang**,[1,2,3] **Yongbing Zhang**,[1,2,3] **Yun Zhang**,[4] **and Taosheng Shen**[1]

[1]*College of Civil Engineering and Architecture, Guangxi University, Nanning 530004, China*
[2]*Guangxi Key Labor1atory of Disaster Prevention and Engineering Safety, Nanning 530004, China*
[3]*Key Laboratory of Disaster Prevention and Structural Safety of Ministry of Education, Nanning 530004, China*
[4]*Guangxi Beitou Highway Construction and Investment Group Co. Ltd., Nanning 530022, China*

Correspondence should be addressed to Tao Yang; yt48440002@163.com

Received 28 January 2021; Revised 25 February 2021; Accepted 2 March 2021; Published 10 March 2021

Academic Editor: Haohui Xin

Steel-concrete composite beams with corrugated steel webs (CSWs) usually have concrete flanges that are prone to crack under tension, and an innovative posttensioned composite beam (IPCB) with CSWs has been proposed previously to overcome this shortcoming. Here, an IPCB with CSWs is manufactured and submitted to a flexural test to investigate its flexural behavior, based on which finite element (FE) models with different parameters are developed and analyzed using the ANSYS software. The effects of the span-to-depth ratio, concrete compressive strength, initial effective prestress, width of the upper concrete flange, and yield strength of the steel tubes on the flexural behavior of the IPCBs with CSWs are discussed. Numerical results show that the span-to-depth ratio of the beam and the yield strength of the steel tube have a considerable effect on the ultimate load-carrying capacity of the IPCB, which increases by 48.2% when the depth of the CSWs is increased from 240 to 400 mm and by 21.8% when the yield strength of the steel tubes is increased from 295 to 395 MPa. The plane-section assumption is unsuitable for IPCBs. Almost all the unbonded posttensioning strands in the beams yield for the specimens at ultimate state. The normal stress is distributed unevenly across the width of the upper concrete flange, and the maximum shear lag coefficient is 1.17. Based on the numerical results, a calculation method is established to evaluate the bending moment resistance of an IPCB with CSWs. Comparison shows that the theoretical results in accordance with the proposed method agree well with the numerical results.

1. Introduction

Bridge engineering has seen the widespread use of steel-concrete composite beams with corrugated steel webs (CSWs), which have the advantages of low deadweight and good load-carrying capacity. Moreover, compared with steel-concrete composite beams with flat steel webs, those with CSWs are more effective for transferring prestressing to the concrete components because the longitudinal stiffness of CSWs is significantly lower than that of flat steel webs. Therefore, the flexural behavior of composite beam with CSWs has been investigated worldwide. Elgaaly et al. [1, 2] investigated experimentally and numerically the flexural behavior of girders with CSWs and found that the contribution of CSWs to the moment carrying capacity can be neglected. Chan et al. [3] conducted finite element (FE) analysis and found that beams with vertical corrugation webs gave a significant enhancement in strength compared with those applied horizontal corrugation and plane webs. Kövesdi et al. [4] developed numerical models to investigate the stress distribution and tendency of additional normal stresses in the flanges of girders with CSWs, and they proposed an enhanced design method to predict the maximal transverse bending moment in the most unfavorable case. Inaam and Upadhyay [5] established an empirical equation to determine the ultimate moment resistance of slender flanges for corrugated girders based on numerical results. Mo et al. [6] carried out cyclic flexural tests on prestressed concrete (PC) bridges with CSWs, and their test results showed that specimen failure initiated from crushing

of the concrete of the upper flange in the midspan. Mori et al. [7] studied numerically the stress distribution of CSWs in PC bridges, and their results showed that stress concentration occurred near the connections between the steel flanges and webs. Liu et al. [8] investigated the flexural behavior of PC girders with CSWs and proposed a way to predict the strength and deformation of the beams. Chen et al. [9] studied numerically and experimentally the behavior of PC bridges with CSWs and revealed that the localized flange plastic hinge is the dominant factor that determines the full-range structural behavior of the bridge. Chen et al. [10, 11] proposed a new type of composite box girder with CSWs and trusses, and their experimental results showed that this type of composite beam has higher yield load and smaller deflection compared with those without concrete-filled steel tubes. He et al. [12] investigated the static and dynamic behavior of a prefabricated composite box girder with CSWs and concrete-filled steel tube slabs, and it is revealed that the girder possessed a sufficient safety margin. Due to the accordion effect of CSWs, the classical beam theory cannot be used to evaluate the behavior of beams with CSWs properly. As a result, some researchers have proposed different assessment methods for the mechanical performance of composite beams with CSWs. Kato et al. [13, 14] considered the shear deformation of CSWs and proposed a practical method for calculating the displacement and section force of composite beam bridges with CSWs. Machimdamrong et al. [15] established an elastic shear deformable beam bending theory (G3 theory) for composite PC girders with CSWs. Bariant et al. [16] proposed the elasto-plastic G3 theory to predict the performance of PC girders with CSWs by accounting for the inelastic properties of the CSWs. Chen et al. [17] developed an extended sandwich theory for PC bridges with CSWs that considered the sectional characteristics as well as the effects of diaphragms. The finite element method proposed by Xin et al. [18] could provide reference for the fatigue life evaluation of composite beams with CSWs also.

Although conventional composite beams with CSWs have superior properties, their concrete flanges are still prone to crack in the tension zone under bending moment, thereby affecting adversely the safety and durability of the structure. Given these problems, Chen et al. [19] proposed an innovative posttensioned composite beam (IPCB) with CSWs, in which concrete-filled steel tubes replace the lower concrete flanges and unbonded posttensioning strands (UPSs) are arranged in the steel tubes. The IPCB with CSWs is shown schematically in Figure 1. In the present study, a reduced-scale IPCB was subjected to a flexural experiment, and FE models were developed to investigate the flexural behavior of IPCBs.

2. Flexural Experiment

2.1. Experimental Design. An IPCB with CSWs was designed, fabricated, and subjected to a four-point bending test under monotonic loading. Its dimensions are shown in Figure 2. The clear span was 6000 mm, the upper concrete flange was 900 mm wide and 80 mm thick, and the top flange of the steel girder was 680 mm wide and 6 mm thick. The lower concrete-filled steel tube was 180 mm wide and 100 mm thick, and the wall thickness was 4 mm. In each steel tube was arranged a UPS with a diameter of 15.2 mm. The ultimate strength f_{ptk} of the UPS was 1860 MPa, and the initial effective prestress was taken as $0.6f_{ptk}$ (1116 MPa). The CSWs and the stiffeners were 4 and 8 mm thick, respectively, and the detailed dimensions of the corrugation profile are shown in Figure 2(c). The average compressive strength of the concrete from three prism specimens (100 mm × 100 mm × 300 mm) was 49.8 MPa. Meanwhile, the material properties of the steel are listed in Table 1.

During the test, the load was applied by a hydraulic jack with a maximum loading capacity of 1500 kN. Wedge-type anchorages were used to anchor the UPSs, and load cells were installed between the anchorages and the beam ends to monitor the internal force variation of the strands. The arrangement of the strain measuring points and displacement meters is shown in Figure 2(a). The monotonic load was distributed to two symmetrical points, and the test ended once the applied load had decreased to being 0.85 times the ultimate load in the declining stage of the load-carrying capacity.

2.2. Observations. During the initial loading stage, no phenomena were observed. As the applied load was increased from 200 to 240 kN, the tested beam was heard to rattle. When the load reached 586.5 kN, the bottom of the steel tube at the midspan section yielded. Afterward, midspan deflection increased rapidly with increasing load. At the ultimate load of 962.3 kN, the upper concrete flange slab in the midspan began to be crushed, and the top flange of the steel girder near the crushed concrete flange buckled locally. Finally, the test ended because of the severe damage to the concrete flange. Figure 3 shows the final failure mode of the specimen, which was typical flexural failure. Buckling failure of the CSWs and tubes was not observed, nor was (i) fracture of the UPSs or (ii) connection failure at the interface between the CSWs and the flanges.

2.3. Load-Carrying Capacity and Deformability. Figure 4 shows the relationship between the applied load and the midspan deflection of the specimen, where P_y and P_u are the yield and ultimate loads, respectively. As can be seen, the deflection increased linearly with the applied load at the initial loading stage. When the load approached 586.5 kN, the bottom surface of the steel tubes near the midspan yielded, and the composite beam gradually became less stiff and entered the elastic-plastic working stage. The ultimate load was of the tested beam 962.3 kN, and the corresponding midspan deflection was 76.1 mm. At this time, the upper concrete flange was crushed locally and the load-carrying capacity dropped rapidly to 817.2 kN.

2.4. Internal Force of UPSs. Figure 4 also illustrates the development of the average internal force of the UPSs in the steel tubes. As can be seen, the internal force increased

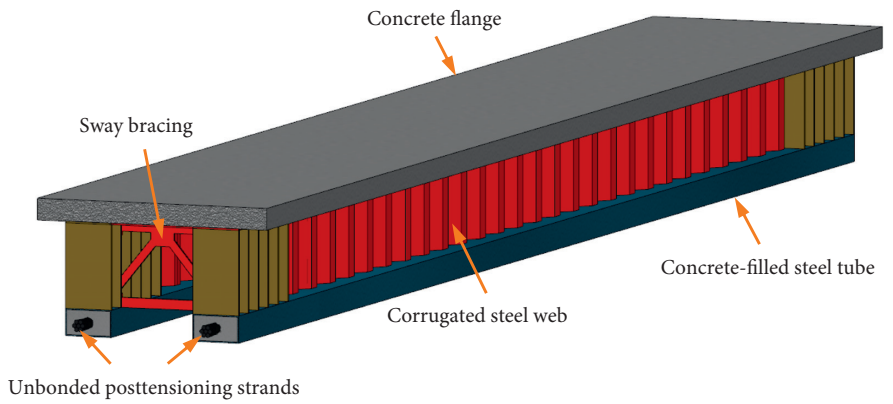

Figure 1: Schematic diagram of innovative posttensioned composite beam (IPCB) with corrugated steel webs (CSWs).

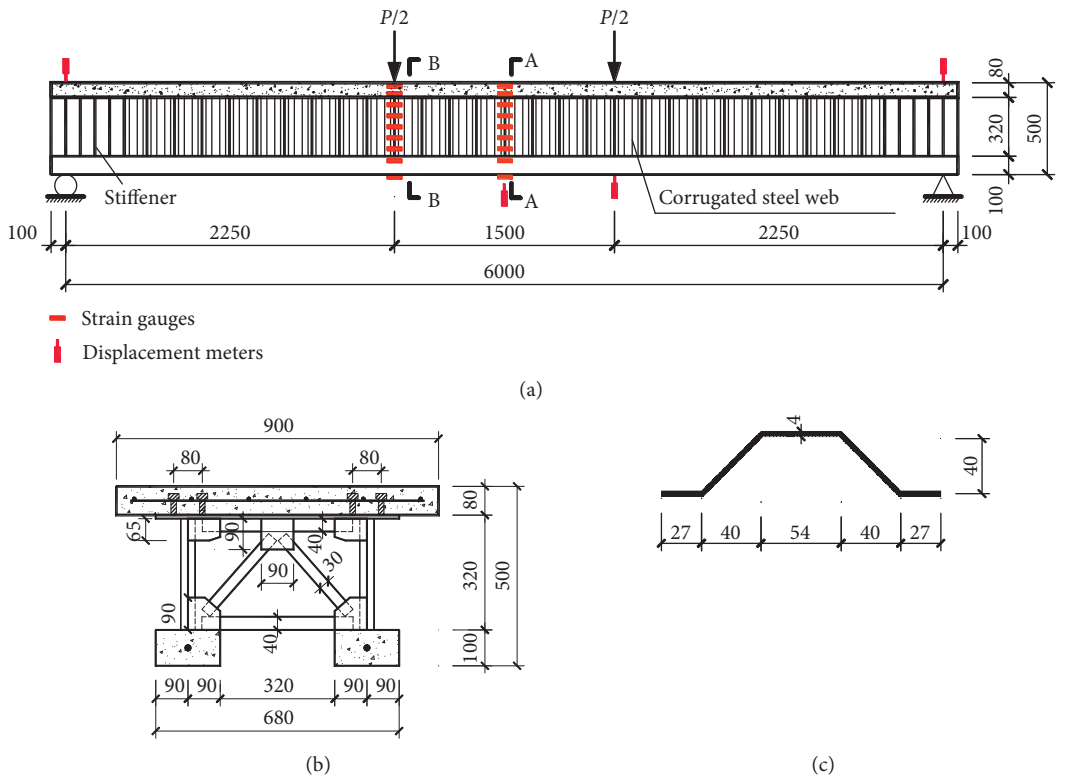

Figure 2: Design of the test specimen. (a) Dimensions and geometry of beam. (b) Sections A-A and B-B. (c) Details of corrugation profile.

Table 1: Material properties of steel.

Material	Yield strength (MPa)	Ultimate tensile strength (MPa)	Elongation (%)
CSW	375	550	30.0
Top flange of steel girder	380	540	31.0
Steel tube	396	535	30.0
Stiffener	365	545	30.5

linearly with the midspan deflection in the initial loading process. Afterward, the growth rate of the internal force decreased after the internal force reached 210.0 kN. When the ultimate load was reached, the internal force for the UPSs was only 219.7 kN, which was less than the ultimate tensile force of 260.4 kN.

3. Finite Element Modeling and Analysis

3.1. Details of FE Beam Model. The commercial software ANSYS was used to develop an FE model (hereinafter referred to as model S0) with the same design parameters as those of the tested beam. The eight-node solid element SOLID65 was used to simulate the concrete, the SHELL181 element was used to simulate the steel webs, flange, tubes, and stiffeners, and the LINK element was used to simulate

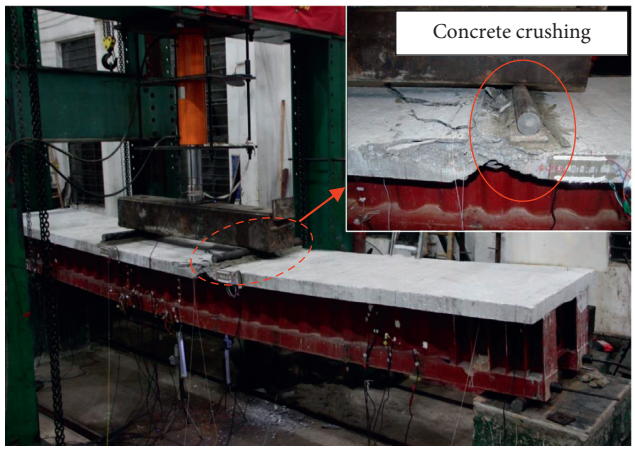

Figure 3: Failure mode of tested beam.

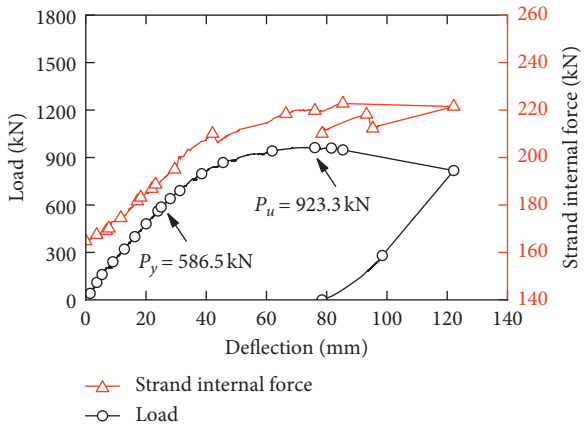

Figure 4: Experimental results.

the reinforcement and UPSs. To avoid stress concentration, steel plates were established at the supports and loading points. Given the lack of bonding force between the UPSs and the concrete, the adjacent element nodes of the strands and concrete were coupled with each other in the beam width and beam depth direction, while their movements in the beam span direction retained freedom. The effective prestress was applied to the UPSs by setting the initial strain as a constant.

3.2. Constitutive Laws. In the model, the concrete was treated as an isotropic and homogeneous material, and its stress-strain constitutive relationship ($\sigma - \varepsilon$) was given by equations (1)–(4) in accordance with the Chinese code for the design of concrete structures [20], where ε_c is the strain corresponding to the concrete compressive strength f_c, n and α_c are the constants defined by equations (2) and (4), respectively, and E_c is the elastic modulus of the concrete. The multilinear isotropic (MISO) hardening model was used to input the constitutive law of concrete. Because the negative slope of the constitutive curve can lead to calculation convergence difficulties, the descending stage of the curve for concrete was substituted by a horizontal line. The ultimate compressive strain of concrete was taken as 0.0033. For the steel, the bilinear kinematic (BKIN) hardening model was used to simulate the constitutive relationship. For the first linear stage, the slope was taken as elastic modulus E_s, while for the second linear stage, the slope was taken as $0.01E_s$. The multilinear kinematic (MKIN) hardening model was used for the UPSs, and the stress-strain relationship ($\sigma_p - \varepsilon_p$) is given by equations (5) and (6) according to [21], where $\sigma_{0.2}$ and E_p are the nominal yield strength and the elastic modulus of the UPSs, respectively:

$$\sigma = \begin{cases} \dfrac{n f_c \varepsilon}{\varepsilon_c \left[n - 1 + (\varepsilon/\varepsilon_c)^n \right]}, & \varepsilon \le \varepsilon_c, \\ \dfrac{f_c \varepsilon}{\varepsilon_c \left[\alpha_c (\varepsilon/\varepsilon_c - 1)^2 + \varepsilon/\varepsilon_c \right]}, & \varepsilon > \varepsilon_c, \end{cases} \tag{1}$$

$$n = \frac{E_c \varepsilon_c}{E_c \varepsilon_c - f_c}, \tag{2}$$

$$\varepsilon_c = \left(700 + 172\sqrt{f_c} \right) \times 10^{-6}, \tag{3}$$

$$\alpha_c = 0.157 f_c^{0.785} - 0.905, \tag{4}$$

$$\varepsilon_p = \frac{\sigma_p}{E_p} + 0.002 \left(\frac{\sigma_p}{\sigma_{0.2}} \right)^{13.5}, \tag{5}$$

$$\sigma_{0.2} = 0.85 f_{ptk}. \tag{6}$$

3.3. Loading Steps and Failure Criteria. The load was applied as a constant displacement on the two loading points during the analysis. The strain distribution and the vertical midspan deflection of the beams were monitored. Once the total normal strain on the top surface of the concrete flange slab reached 0.0033, flexural failure was deemed to have occurred.

3.4. Validation. Figure 5 shows the distribution of total normal strain in the FE model S0 along the beam span at final failure. As can be seen, the strain of the upper concrete flange in the pure flexural region was larger than that in the flexure-shear region. The maximum strain appeared mainly near the loading points, which withstood the combined action of shear and flexure. Comparison of Figures 3 and 5 showed that the FE model S0 had the same failure mode as the tested IPCB. Figures 6 and 7 illustrate the comparison of the experimental curves and the numerical results. As can be seen, the curves agree well with each other. In general, the proposed modeling method can be used to evaluate the flexural behavior of IPCBs.

3.5. Parametric Analysis. FE models were built to evaluate how the flexural behavior of an IPCB is influenced by (i) the span-to-depth ratio, (ii) the concrete compressive strength, (iii) the initial effective prestress, (iv) the width

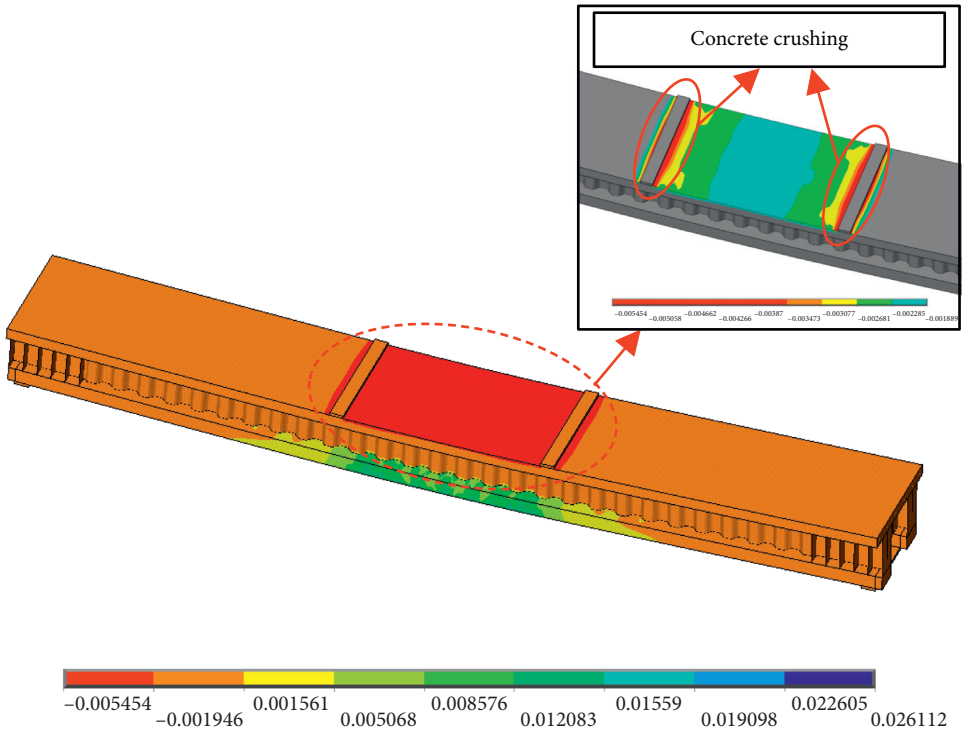

Figure 5: Failure mode of FE model S0.

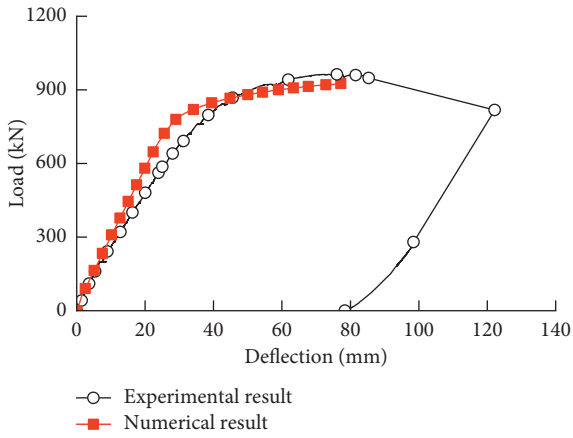

Figure 6: Load-deflection curve.

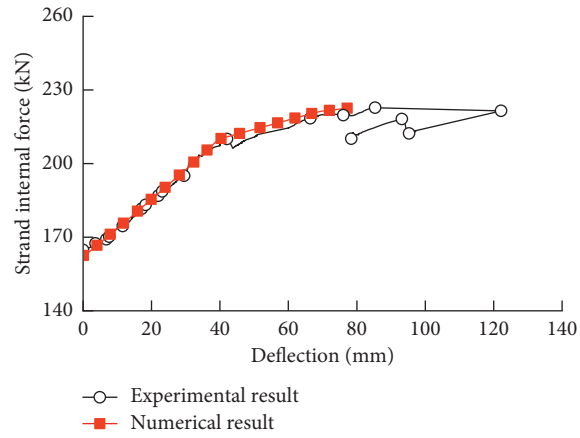

Figure 7: Strand internal force vs. midspan deflection.

of the upper concrete flange, and (v) the yield strength of the steel tubes. The designs of the FE models are listed in Table 2, where b is the width of the upper concrete flange, h_w is the CSW depth, l is the total length of the beam, σ_{pe} is the initial effective prestress of the UPSs, and f_y is the yield strength of the steel tubes.

The models were established and analyzed using the FE method proposed above, and the main numerical results are listed in Table 3, where P_y and P_u are the yield and ultimate loads, respectively, of the beam, and Δ_y and Δ_u are the midspan deflections corresponding to P_y and P_u, respectively. The effects of different parameters on the flexural behavior of the IPCBs were discussed as follows.

Figure 8 shows the load versus the midspan deflection of the IPCBs with different span-to-depth ratios. As shown in Figure 8(a), the ultimate load-carrying capacity of S2 was 627.6 kN, and those of S1 and S3 were greater by 23.3% and 48.2%, respectively. This indicates that the bending moment resistance of the IPCBs increased with increasing CSW depth when the beam span was kept constant. According to Figure 8(b), the ultimate load-carrying capacity of S1 was 1.40 and 1.83 times those of S4 and S5, respectively. In general, the ultimate load-carrying capacity of the IPCBs tended to decrease with increasing span-to-depth ratio, while the deformability presented the opposite trend.

According to Figure 9, the yield strength of the steel tubes is one of the main factors affecting the ultimate load-

Table 2: Details of FE models in parametric analysis.

Model ID	b (mm)	h_w (mm)	l (mm)	f_c (MPa)	σ_{pe} (MPa)	f_y (MPa)
S1	900	320	6200	32.4	1116	345
S2	900	240	6200	32.4	1116	345
S3	900	400	6200	32.4	1116	345
S4	900	320	8080	32.4	1116	345
S5	900	320	9960	32.4	1116	345
S6	900	320	6200	29.6	1116	345
S7	900	320	6200	38.5	1116	345
S8	900	320	6200	32.4	930	345
S9	900	320	6200	32.4	1302	345
S10	1000	320	6200	32.4	1116	345
S11	1100	320	6200	32.4	1116	345
S12	900	320	6200	32.4	1116	295
S13	900	320	6200	32.4	1116	395

Table 3: Primary numerical results.

Model ID	P_y (kN)	Δ_y (mm)	P_u (kN)	Δ_u (mm)	Curvature ($\times 10^{-5}$/mm)
S1	567.8	20.4	773.7	72.5	3.27
S2	428.4	22.8	627.6	78.2	3.82
S3	681.8	17.6	930.1	64.2	2.78
S4	378.4	30.0	552.3	99.6	3.02
S5	285.3	42.5	423.2	146.8	4.37
S6	554.7	20.4	748.4	61.2	2.67
S7	561.1	19.7	799.1	82.8	4.03
S8	552.3	19.9	778.5	71.9	3.18
S9	556.0	19.7	779.9	65.0	2.79
S10	533.4	18.6	796.8	73.8	3.58
S11	556.9	19.1	808.2	79.6	3.71
S12	483.3	17.1	696.0	79.3	3.67
S13	630.1	22.8	848.5	65.2	2.77

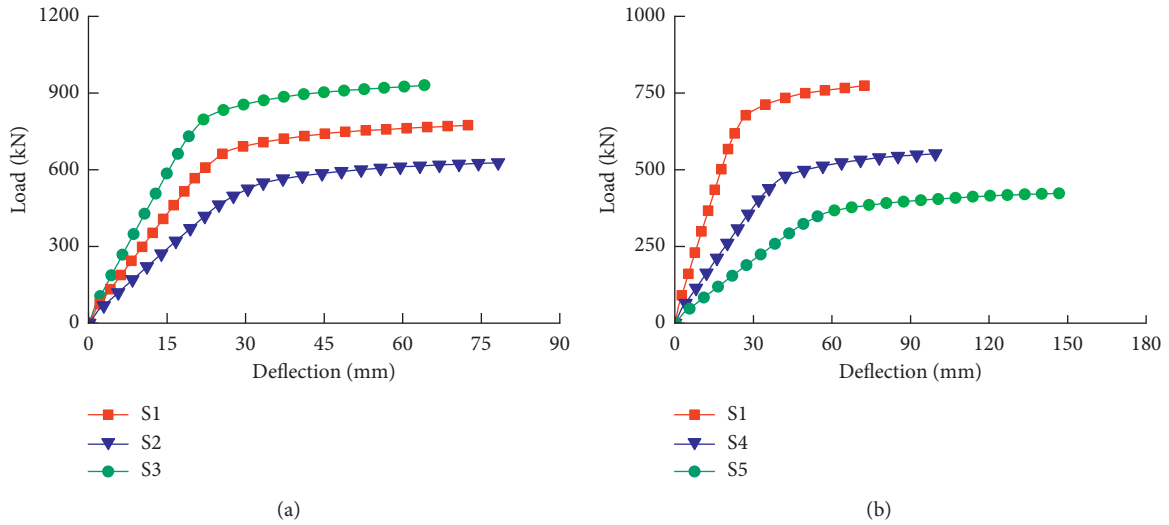

Figure 8: Load vs. midspan deflection with different span-to-depth ratios. (a) Effect of CSW depth. (b) Effect of beam span.

carrying capacity of an IPCB. It can be found that the curves of load versus midspan deflection for the three specimens overlapped approximately at the initial loading stage. With increasing load, the steel tubes of S12 yielded first, causing a notable decrease in beam stiffness and a rapid increase in midspan deflection. At the later loading stage, the curves of load versus midspan deflection were parallel to each other. The ultimate load-carrying capacities of S13 and S1

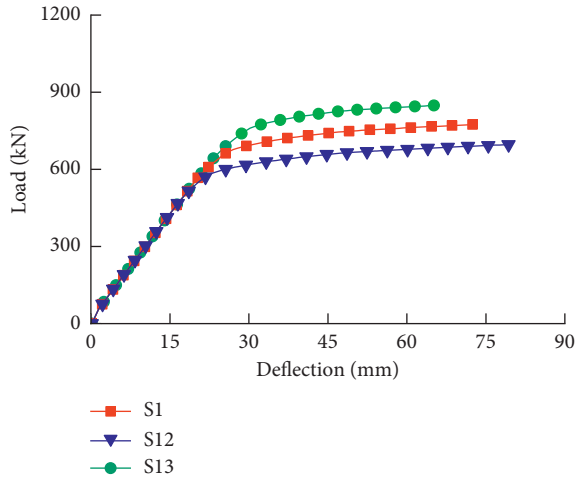

Figure 9: Load vs. midspan deflection with different yield strengths of steel tubes.

increased by 21.8% and 11.2%, respectively, compared with S12, while the midspan deflections of S13 and S1 at ultimate state decreased by 17.8% and 8.6%, respectively, compared with S12. Therefore, using steel tubes with higher yield strength would improve the IPCB load-carrying capacity.

Figure 10 shows the curves of load versus midspan deflection for specimens S1, S6, and S7 with different concrete compressive strengths. As can be seen, the ultimate load-carrying capacity increased by only 6.8% when the concrete compressive strength was increased from 29.6 to 38.5 MPa. However, the midspan deflections of the specimens at ultimate state increased obviously.

S1, S8, and S9 were designed to evaluate the effect of the initial effective prestress of the UPSs. Figure 11 shows that when the initial effective prestress was taken as $0.5f_{ptk}$, $0.6f_{ptk}$, and $0.7f_{ptk}$, respectively, the ultimate load-carrying capacity and deformability of the IPCBs were nearly the same. It is concluded that the initial effective prestress of the UPSs has little effect on the flexural behavior of an IPCB with CSWs.

S1, S10, and S11 were designed to evaluate the effect of the width of the upper concrete flange. Figure 12 shows that the ultimate load-carrying capacities of S10 and S11 were 1.03 and 1.04 times that of S1, and there was little difference in the ultimate deformability. Therefore, the width of the upper concrete flange affects the ultimate load-carrying capacity and deformability of the IPCB slightly.

4. Flexural Characteristics of IPCBs

4.1. Strain Distribution of Beam Section. Based on the above FE analysis, the characteristics of the strain distribution through the depth of beam sections are summarized and the representative curves are shown in Figure 13, taking S1 as an example. As can be seen, the plane-section assumption is no longer valid. The normal strain of the CSWs approached zero in the beam section except for the local zones connecting with the upper and lower flanges. In addition, the normal strain was distributed almost linearly through the depth of the upper and lower flanges. When the applied load

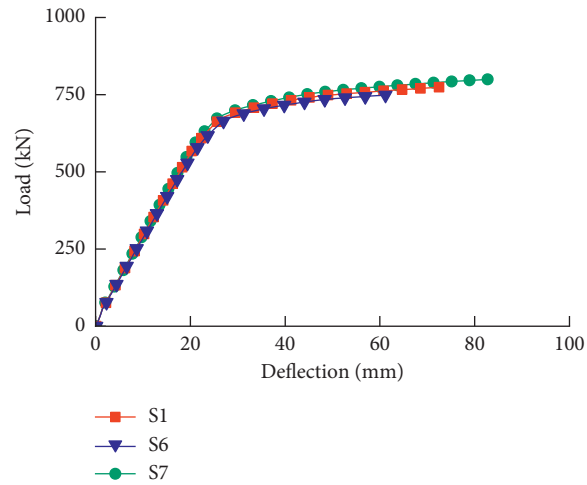

Figure 10: Load vs. midspan deflection with different concrete compressive strengths.

was less than $0.8P_u$, the strain distribution curves of normal strain in sections A-A and B-B, marked in Figure 2(a), presented different characteristics, as shown in Figure 13. For section A-A, the upper and lower flanges produced the same rotation angles, and their normal strain distributions were nearly collinear. Meanwhile, the normal strain distributions of the upper and lower flanges for section B-B were parallel to each other. The different strain distributions for the two sections were due mainly to the shear force. When the applied load reached the ultimate load-carrying capacity, the two distribution curves in each section were parallel to each other.

4.2. Stress Development of UPSs. Figure 14 illustrates the stress development of the UPSs. The curves can be divided into two stages. In the first stage, the UPS stress increased linearly with the midspan deflection until the total UPS stress reached $0.8f_{ptk}$, i.e., 1488 MPa, after which the slope of the curves decreased obviously. It can be seen from Figure 13 that using higher CSWs and shorter beam spans

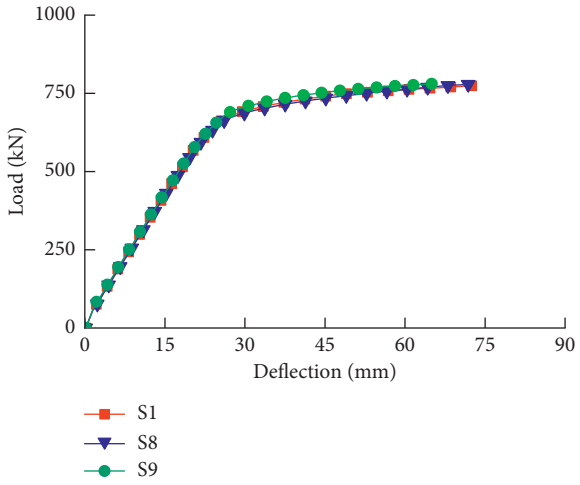

Figure 11: Load vs. midspan deflection with different initial effective prestress.

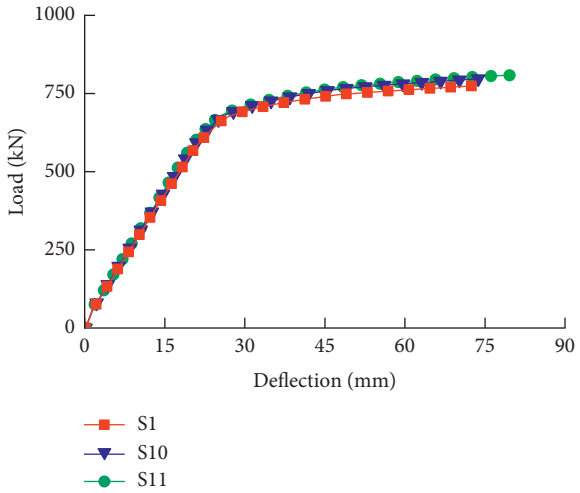

Figure 12: Load vs. midspan deflection with different widths of upper concrete flange.

led to a rapid increase in UPS stress. However, the UPS stress increment was affected only slightly by the concrete compressive strength and the initial effective prestress of the UPSs. In general, the total UPS stress at ultimate state was between 1509.8 and 1588.6 MPa based on the numerical analysis. Because the nominal UPS yield strength was 1581 MPa, in all the FE models the UPSs were about to yield at ultimate state.

4.3. Distribution of Shear Lag Coefficient along Transverse Direction. Steel-concrete composite beams are usually subjected to shear lag; i.e., the normal stress along the width of the flanges is distributed unevenly. To assess this characteristic, the shear lag coefficient $\lambda = \sigma/\sigma_E$ is defined by

$$\sigma_E = \frac{\int_0^b \sigma \, dz}{b}, \tag{7}$$

where σ_E is the average normal stress along the width of the upper concrete flange.

Numerical results indicated that the shear lag coefficients of all the IPCBs had similar distribution characteristics. Therefore, S1 and S11 were chosen as examples to illustrate the distribution law of the shear lag coefficient, as shown in Figure 15. It can be seen that when the applied load was less than $0.8P_u$, the shear lag in section B-B was more evident than that in section A-A. When the applied load reached $1.0P_u$, the shear lag in both sections became conspicuous. The maximum shear lag coefficient of section B-B was 9.8% higher than that of section A-A at final failure, and this was because of the shear force. Because the maximum shear lag coefficient of the calculated IPCBs was 1.17, the adverse influence of the stress concentration near the connections of the CSWs and concrete flanges should be considered in the flexural design.

4.4. Moment-Curvature Curves. Numerical results showed that the curves of bending moment versus curvature for the FE model beams were similar, and the typical moment-curvature curves at section A-A are shown in Figure 16. As can be seen, the sectional deformability was closely connected with the CSW depth and the yield strength of the steel tubes. The sectional curvatures of section A-A at final failure are listed in Table 2, where it can be seen that the sectional curvature varied between 2.67×10^{-5}/mm and 4.37×10^{-5}/mm.

The degeneration law of the sectional rigidity for the IPCBs can be obtained from the moment-curvature curves. The normalized moment-sectional rigidity curves are shown in Figure 17(a), where K_0 and K are the equivalent initial flexural rigidity and the secant flexural rigidity, respectively, of the composite beam section, and M_u and M are the ultimate bending moment resistance and the actual moment at any section, respectively. Because the normalized curves presented similar trends, a mathematical model of the sectional rigidity degeneration is proposed as shown in Figure 17(b) and expressed by equation (8).

$$\frac{K}{K_0} = \begin{cases} 1, & 0 \le \dfrac{M}{M_u} \le 0.75, \\ 1.00 - \left(\dfrac{M}{M_u} - 0.75\right), & 0.75 < \dfrac{M}{M_u} \le 0.85, \\ 0.85 - 4\left(\dfrac{M}{M_u} - 0.85\right), & 0.85 < \dfrac{M}{M_u} \le 1. \end{cases} \tag{8}$$

5. Simplified Method for Calculating Bending Moment Resistance for IPCBs

5.1. Basic Assumptions. From the experimental and numerical results, the following assumptions were used in evaluating the bending moment resistance of the IPCBs. (1) The assumption that the plane beam section remains plane after loading is discarded. The normal strain distribution

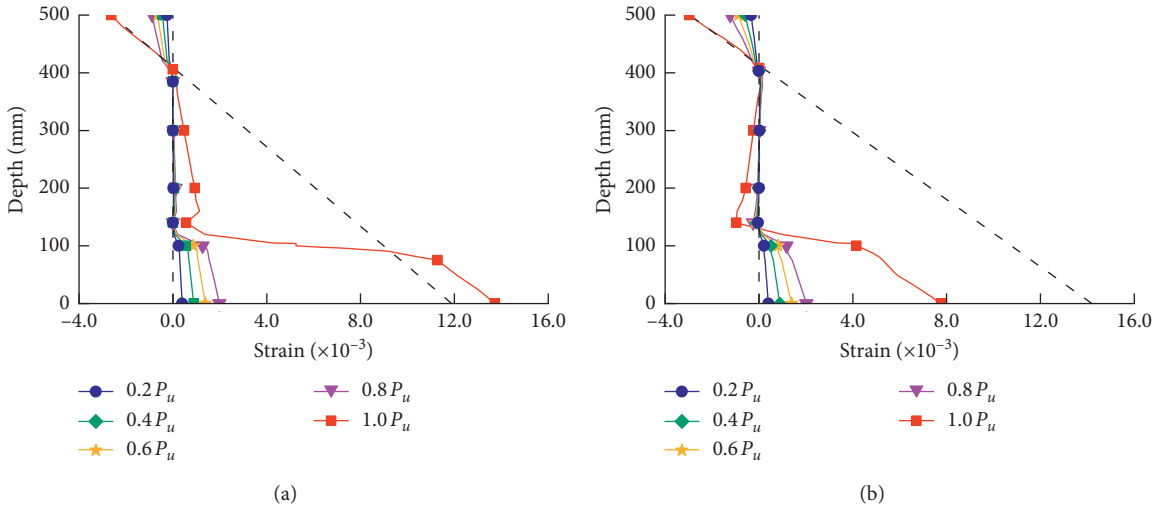

Figure 13: Strain distributions through beam sections of S1: (a) section A-A; (b) section B-B.

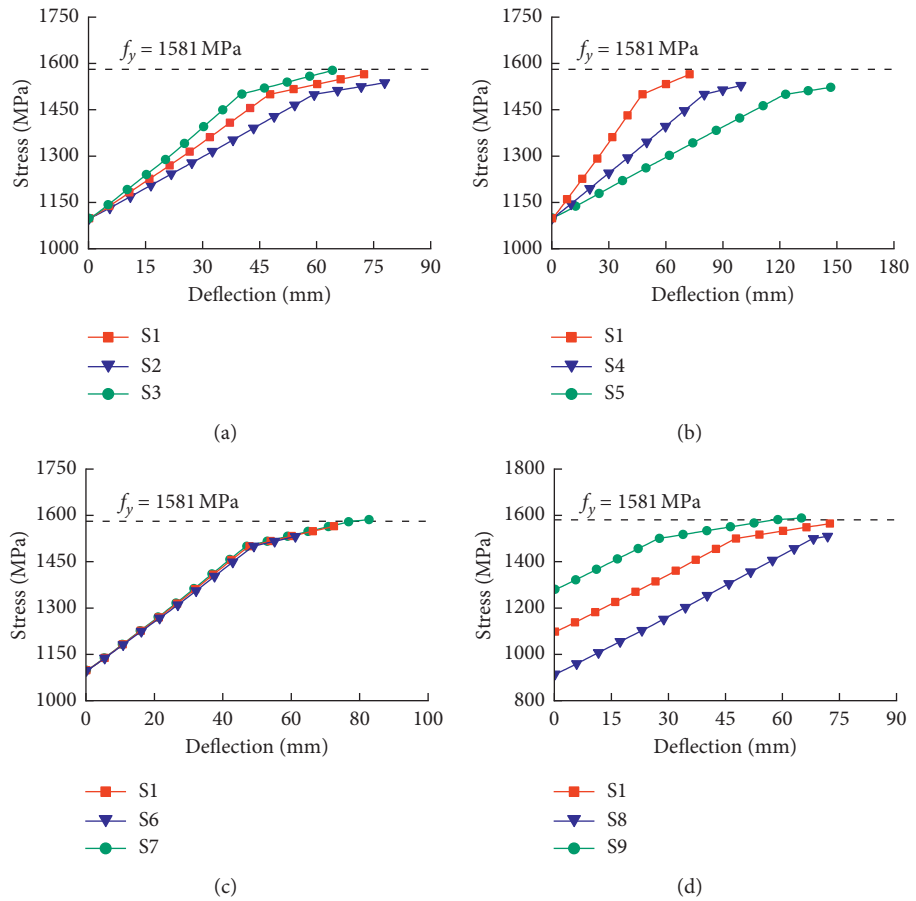

Figure 14: Stress development of UPSs. (a) Effect of CSW depth. (b) Effect of beam span. (c) Effect of concrete compressive strength. (d) Effect of initial effective prestress.

through the depth of the upper and lower flanges remains linear, and the upper concrete flange and the lower concrete-filled steel tube have similar sectional rotation around their own centroid axes. (2) The CSWs work in coordination with the upper and lower flanges, and the possible tiny relative slip and shear connection failure at the interface between the CSWs and the flanges are neglected. (3) The influence of the tensile strength of the concrete and CSWs on the bending

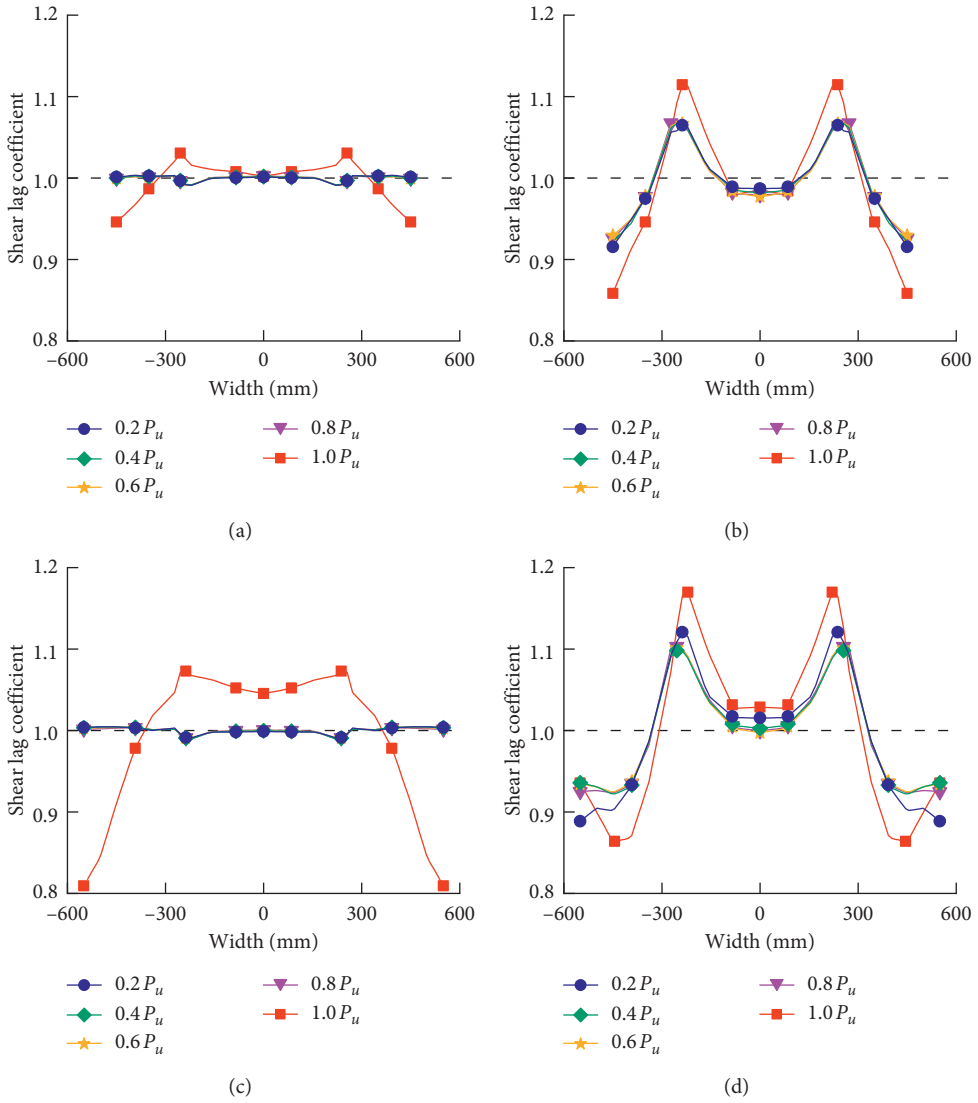

Figure 15: Distribution of shear lag coefficient. (a) Section A-A for S1. (b) Section B-B for S1. (c) Section A-A for S11. (d) Section B-B for S11.

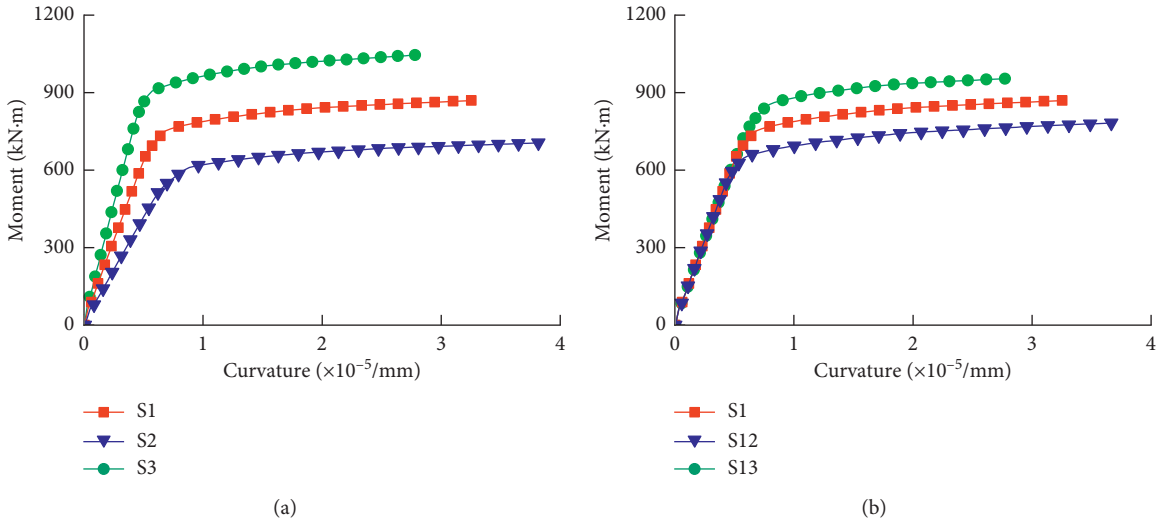

Figure 16: Typical moment-curvature curves. (a) Effect of CSW depth. (b) Effect of yield strength of steel tubes.

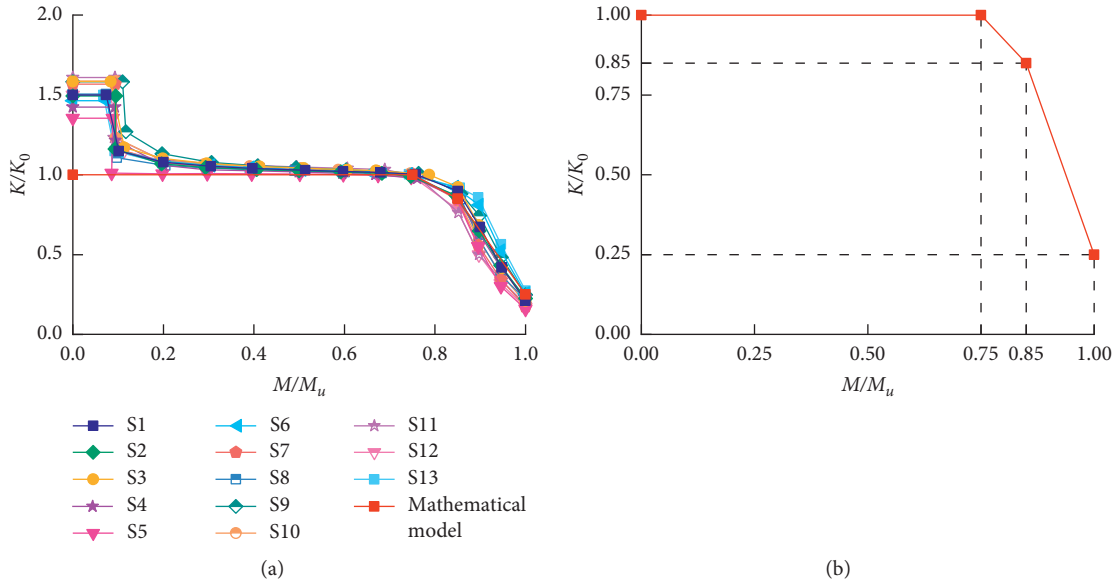

Figure 17: Relationship between moment and sectional rigidity. (a) Normalized curves. (b) Mathematical model.

moment resistance is neglected. (4) The constitutive relationship of the UPSs is described by equations (5) and (6). (5) The enhanced strength of the steel tubes from being filled with concrete is not considered. (6) Shear deformation is not considered when calculating the UPS strain increment.

5.2. Theoretical Models. To evaluate the bending moment resistance of an IPCB, the first step is to determine the UPS stress under the bending moment. According to [22], the UPS strain increment can be expressed as

$$\Delta\varepsilon_p = \frac{\Delta l_p}{l_p} = \frac{\int_0^{l_0} e(x) f''(x)\,\mathrm{d}x}{l_p}, \tag{9}$$

where Δl_p is the total UPS elongation, l_p is the total UPS length, l_0 is the clear span of the beam, $f(x)$ is the beam deflected shape, and $e(x)$ is the UPS eccentricity relative to the neutral axis of the beam section.

For flexural members, the curvature $\phi(x)$ can be given approximately by

$$f''(x) \approx \phi(x) = \frac{M(x)}{B(x)}, \tag{10}$$

where $M(x)$ is the bending moment at any section and $B(x)$ is the corresponding secant flexural rigidity of the section.

For the IPCBs studied herein, $e(x)$ is a constant e_m because the UPSs are arranged in a straight line along the beam. Therefore, $\Delta\varepsilon_p$ can be expressed as follows by combining equations (9) and (10):

$$\Delta\varepsilon_p \approx \frac{e_m}{l_p}\int_0^{l_0} \frac{M(x)}{B(x)}\,\mathrm{d}x. \tag{11}$$

The bending moment diagram for a simply supported IPCB under ultimate load P_u is shown in Figure 18. According to equations (8) and (11), the composite beam can be divided into parts 1–4 to calculate $\Delta\varepsilon_p$ at ultimate state:where $B_1(x)$, $B_2(x)$, $B_3(x)$, and $B_4(x)$ are the secant flexural rigidity in each part. To simplify equation (12), the average secant flexural rigidity is introduced to substitute the varying secant flexural rigidity in each part. Thus, the secant flexural rigidity in each part can be expressed conveniently as

$$\begin{aligned}\Delta\varepsilon_p &= \frac{e_m}{l_p}\int_0^{l_0}\frac{M(x)}{B(x)}\,\mathrm{d}x \\ &= \frac{2e_m}{l_p}\left[\int_0^{0.75a}\frac{M(x)}{B_1(x)}\,\mathrm{d}x + \int_{0.75a}^{0.85a}\frac{M(x)}{B_2(x)}\,\mathrm{d}x + \int_{0.85a}^{a}\frac{M(x)}{B_3(x)}\,\mathrm{d}x + \int_a^{0.5l_0}\frac{M(x)}{B_4(x)}\,\mathrm{d}x\right],\end{aligned} \tag{12}$$

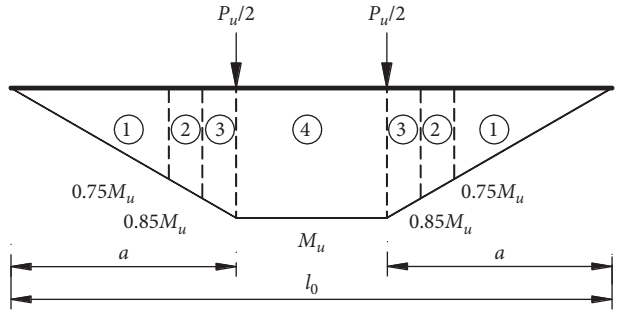

Figure 18: Bending moment diagram.

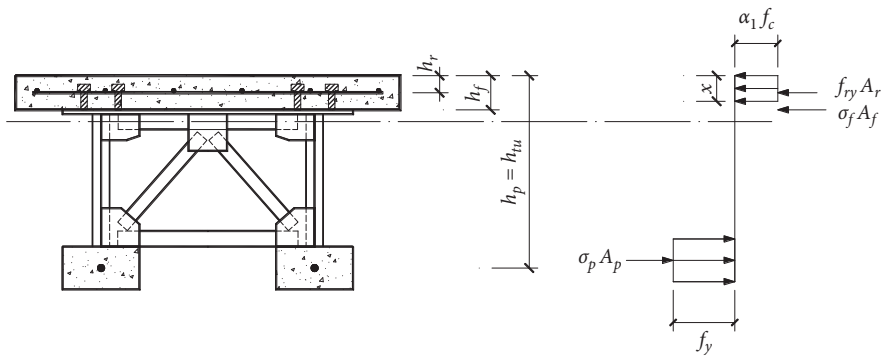

Figure 19: Calculation model for analyzing flexural performance.

$$\begin{cases} B_1(x) = K_0, & 0 \le M(x) \le 0.75M_u, \\ B_2(x) = 0.925K_0, & 0.75M_u < M(x) \le 0.85M_u, \\ B_3(x) = 0.55K_0, & 0.85M_u < M(x) < M_u, \\ B_4(x) = 0.25K_0, & M(x) = M_u. \end{cases} \tag{13}$$

Combining equations (12) and (13) gives $\Delta\varepsilon_p$, whereupon the total UPS strain ε_p at ultimate state is given as

$$\varepsilon_p = \varepsilon_{pe} + \Delta\varepsilon_p, \tag{14}$$

where ε_{pe} is the initial effective UPS strain. Thus, the total UPS stress σ_p at ultimate state can be obtained.

The diagram for calculating the bending moment resistance of the IPCB with CSWs is shown in Figure 19, and the force equilibrium at ultimate state is given as

$$\sigma_p A_p + f_y A_{tu} = \alpha_1 f_c b x + \sigma_f A_f + f_{ry} A_r, \tag{15}$$

where σ_f is the total stress of the top flange of the steel girder, f_{ry} is the yield strength of the reinforcement, A_p, A_{tu}, A_f, and A_{ry} are the areas of the UPSs, steel tubes, steel flange, and reinforcement, respectively, α_1 is the reduction factor of concrete compressive strength (taken here as 1.0), b is the width of the upper concrete flange, and x is the depth of the stress block.

Meanwhile, the bending moment resistance M_u can be expressed as

$$\begin{aligned} M_u = {} & \sigma_p A_p \left(h_p - \frac{x}{2}\right) + f_y A_{tu} \left(h_{tu} - \frac{x}{2}\right) \\ & - \sigma_f A_f \left(h_f - \frac{x}{2}\right) - f_{ry} A_r \left(h_r - \frac{x}{2}\right), \end{aligned} \tag{16}$$

where h_p, h_{tu}, h_f, and h_r are the distances from the resultant forces of the UPSs, steel tubes, top steel flange, and reinforcement, respectively, to the concrete extreme fiber in compression. Because the reinforcement and the steel flange are very close to the centroid axis of the compression zone, the contribution to the bending moment resistance is neglected in the following calculation.

According to equations (12) and (13), M_u should be calculated first to determine $\Delta\varepsilon_p$. However, it is difficult to obtain M_u directly by equations (5), (6), and (12) through (16). To increase the applicability of the proposed method, M_u is computed iteratively. First, assuming $\sigma_p = \sigma_{pe}$, the first bending moment resistance M_{u_1} is obtained according to equations (15) and (16). Second, σ_p is recalculated by substituting M_{u_1} into equation (12), and the second bending moment resistance M_{u_2} is obtained. These steps are repeated until the two adjacent values of the bending moment resistance satisfy the required error tolerance. Based on the proposed simplified calculation method, the iterative operation was performed only twice before satisfactory calculation results were obtained for the FE models investigated herein. Table 4 lists the results M_{u_1} and M_{u_2} of the two iterations and the numerical results of the bending moment

Table 4: Comparison of theoretical and FE results.

Model ID	M_{u_1} (kN·m)	M_{u_2} (kN·m)	M_e (kN·m)	M_{u1}/M_e	M_{u2}/M_e
S1	759.8	802.7	869.7	87.4%	92.3%
S2	614.7	649.0	705.4	87.1%	92.0%
S3	905.0	956.7	1045.4	86.6%	91.5%
S4	759.8	799.7	880.3	86.3%	90.8%
S5	759.8	796.0	873.5	87.0%	91.1%
S6	754.5	796.9	841.2	89.7%	94.7%
S7	768.8	812.7	898.2	85.6%	90.5%
S8	739.3	784.6	875.0	84.5%	89.7%
S9	779.6	808.5	876.6	88.9%	92.2%
S10	765.5	809.3	895.6	85.5%	90.4%
S11	770.1	814.7	908.4	84.8%	89.7%
S12	674.6	716.2	782.3	86.2%	91.5%
S13	843.4	887.0	953.7	88.4%	93.0%

resistance M_e. Comparison shows that the theoretical results M_{u_2} agree well with the numerical results M_e, with the maximum error being less than 10.3%.

6. Conclusions

Herein, the flexural behavior of IPCBs with CSWs was investigated experimentally and numerically, and the following conclusions are drawn.

(1) An IPCB with CSWs was subjected to a flexural test, and the experimental results showed that flexural failure occurred eventually, with the IPCB presenting excellent flexural behavior. Fracture of the UPSs and connection failure at the interface between the CSWs and the flanges were not observed.

(2) Numerical results showed that the span-to-depth ratio and the yield strength of the steel tubes had a significant effect on the ultimate load-carrying capacity of the IPCB with CSWs, which improved by 48.2% when the CSW depth was increased from 240 to 400 mm and by 21.8% when the yield strength of the steel tubes was increased from 295 to 395 MPa. The effective prestress had little effect on the load-carrying capacity of the IPCB with CSWs at the specific UPSs ratio.

(3) The plane-section assumption was unsuitable for the IPCBs with CSWs, but the normal strain distribution through the depth of the upper and lower flanges remained linear. The stress of UPSs increased linearly with increasing midspan deflection at different loading stages, and the UPSs nearly all yielded at final failure of the beam. Shear lag existed in the concrete flanges of the IPCBs with CSWs, and the maximum shear lag coefficient was 1.17. Stress concentration near the connections of the CSWs and concrete flanges should be considered in the flexural design.

(4) A simplified method was proposed for calculating the bending moment resistance of an IPCB with CSWs. The theoretical results M_{u_2} so obtained agreed well with the numerical results M_e, with the maximum error being less than 10.3%.

Data Availability

The data included in this study are available from the corresponding author upon request.

Conflicts of Interest

The authors declare that they have no conflicts of interest regarding the publication of this paper.

Acknowledgments

This research was supported by the National Natural Science Foundation of China (grant no. 51868004) and the Guangxi Key Research and Development Project (grant no. AB19245017).

References

[1] M. Elgaaly, A. Seshadri, and R. W. Hamilton, "Bending strength of steel beams with corrugated webs," *Journal of Structural Engineering*, vol. 123, no. 6, pp. 772–782, 1997.

[2] M. Elgaaly and A. Seshadri, "Depicting the behavior of girders with corrugated webs up to failure using non-linear finite element analysis," *Advances in Engineering Software*, vol. 29, no. 3-6, pp. 195–208, 1998.

[3] C. L. Chan, Y. A. Khalid, B. B. Sahari, and A. M. S. Hamouda, "Finite element analysis of corrugated web beams under bending," *Journal of Constructional Steel Research*, vol. 58, no. 11, pp. 1391–1406, 2002.

[4] B. Kövesdi, B. Jáger, and L. Dunai, "Stress distribution in the flanges of girders with corrugated webs," *Journal of Constructional Steel Research*, vol. 79, pp. 204–215, 2012.

[5] Q. Inaam and A. Upadhyay, "Flexural behaviour of steel I-girder having corrugated webs and slender flanges," *Structures*, vol. 27, pp. 12–21, 2020.

[6] Y. L. Mo, C.-H. Jeng, and H. Krawinkler, "Experimental and analytical studies of innovative prestressed concrete box-girder bridges," *Materials and Structures*, vol. 36, no. 2, pp. 99–107, 2003.

[7] S. Mori, T. Miyoshi, H. Katoh, N. Nishimura, and S. Nara, "A study on local stresses of corrugated steel webs in PC bridges under prestressing," *Technical Memorandum of Public Works Research Institute*, vol. 4009, pp. 449–458, 2006.

[8] X.-G. Liu, J.-S. Fan, J.-G. Nie, Y. Bai, Y.-x. Han, and W.-h. Wu, "Experimental and analytical studies of prestressed concrete girders with corrugated steel webs," *Materials and Structures*, vol. 48, no. 8, pp. 2505–2520, 2015.

[9] X. C. Chen, Y. Zeng, F. T. K. Au, and R. J. Jiang, "Interaction of plastic hinges in prestressed concrete bridges with corrugated steel webs," *Engineering Structures*, vol. 150, pp. 359–372, 2017.

[10] Y. Chen, J. Dong, and T. Xu, "Composite box girder with corrugated steel webs and trusses - a new type of bridge structure," *Engineering Structures*, vol. 166, pp. 354–362, 2018.

[11] Y. Chen, J. Dong, Z. Tong, R. Jiang, and Y. Yue, "Flexural behavior of composite box girders with corrugated steel webs and trusses," *Engineering Structures*, vol. 209, Article ID 110275, 2020.

[12] J. He, Y. Liu, S. Wang, H. Xin, H. Chen, and C. Ma, "Experimental study on structural performance of prefabricated composite box girder with corrugated webs and steel tube slab," *Journal of Bridge Engineering*, vol. 24, no. 6, Article ID 04019047, 2019.

[13] H. Kato, A. Kawabata, and N. Nishimura, "Practical calculation formula on displacements and stress resultants of steel-concrete mixed girders with corrugated steel web," *Doboku Gakkai Ronbunshu*, vol. 2002, no. 703, pp. 293–300, 2002, in Japanese.

[14] H. Kato and N. Nishimura, "Practical analysis of continuous girders and cable stayed bridges with corrugated steel web," *Doboku Gakkai Ronbunshu*, vol. 2003, no. 731, pp. 231–245, 2002, in Japanese.

[15] C. Machimdamrong, E. Watanabe, and T. Utsunomiya, "Analysis of corrugated steel web girders by an efficient beam bending theory," *Structural Engineering/Earthquake Engineering*, vol. 21, no. 2, pp. 131S–142S, 2004.

[16] J.-F. Bariant, T. Utsunomiya, and E. Watanabe, "Elasto-plastic analysis of PC girder with corrugated steel web by an efficient beam theory," *Structural Engineering/Earthquake Engineering*, vol. 23, no. 2, pp. 257s–268s, 2006.

[17] X. Chen, F. T. K. Au, Z. Bai, and Y. Zeng, "An extended sandwich theory for prestressed concrete bridges with corrugated steel web (s)," *IABSE Conference. International Association for Bridge and Structural Engineering*, vol. 104, no. 17, pp. 1–8, 2015.

[18] H. Xin, J. A. Correia, and M. Veljkovic, "Three-dimensional fatigue crack propagation simulation using extended finite element methods for steel grades S355 and S690 considering mean stress effects," *Engineering Structures*, vol. 227, Article ID 111414, 2021.

[19] Q. Chen, Z. Xu, T. Hao, and B. Li, "Prestress introduction efficiency of composite beam with corrugated web and internal prestress," *China Civil Engineering Journal*, vol. 50, no. 12, pp. 72–79, 2017, in Chinese.

[20] MOHURD, *Code for Design of Concrete Structures GB 50010-2010*, Architecture and Building Press, Beijing, China, 2011, in Chinese.

[21] Z. Guo, *Principles of Reinforced Concrete*, Tsinghua University Press, Beijing, China, 1999, in Chinese.

[22] Z.-Q. He and Z. Liu, "Stresses in external and internal unbonded tendons: unified methodology and design equations," *Journal of Structural Engineering*, vol. 136, no. 9, pp. 1055–1065, 2010.